fluids

MDPI

Article

Thermal Performance Analysis of LOX/LCH4 Engine Feed Systems Using CFD Modeling

Iram Hernandez [1], Salvador Orozco [1], Md Amzad Hossain [1,*] and Ahsan Choudhuri [2]

[1] Aerospace Center, The University of Texas at El Paso (UTEP), El Paso, TX 79968, USA; idhernandez2@miners.utep.edu (I.H.); sorozco10@miners.utep.edu (S.O.)
[2] Aerospace and Mechanical Engineering Department, The University of Texas at El Paso (UTEP), El Paso, TX 79968, USA; ahsan@utep.edu
* Correspondence: mhossain12@utep.edu

Abstract: This study examines the thermal management of the Centennial Restartable Oxygen Methane Engine (CROME) feed system under two propellant tank pressure conditions: 33 psi (227.5 kPa) and 100 psi (689.5 kPa), at a constant liquid methane flow rate of 0.9 lbm/s (0.4 kg/s). Using the Eulerian Single-Phase (ESP) model, the initial test validated experimental data, showing close agreement in total pressure (experimental: 31 psi; CFD: 33 psi) and temperature measurements (experimental: −287.3 °F and −300 °F; CFD: −299 °F and −294 °F) with deviations of 6.4% and ≤4.1%, respectively. For the second test, a simplified Volume of Fluid (VOF) model was used, adjusted for varying liquid-to-gas volume fractions. The best agreement with experimental data was found with 100% GN2, showing a 3.1 psi pressure rise and a 3.3% error. These findings show the importance of improving thermal management and precision control in cryogenic LOX-LCH4 feedline systems for optimal engine performance. Future research will focus on exploring pressures up to the propellant tank's maximum rated limit of 400 psi.

Keywords: LOX/LCH4; space propulsion; digital modeling; cryo-feed system; computational analysis



Received: 23 December 2024
Revised: 27 February 2025
Accepted: 4 March 2025
Published: 5 March 2025

Citation: Hernandez, I.; Orozco, S.; Hossain, M.A.; Choudhuri, A. Thermal Performance Analysis of LOX/LCH4 Engine Feed Systems Using CFD Modeling. *Fluids* **2025**, *10*, 62. https://doi.org/10.3390/fluids10030062

Copyright: © 2025 by the authors. Licensee MDPI, Basel, Switzerland. This article is an open access article distributed under the terms and conditions of the Creative Commons Attribution (CC BY) license (https://creativecommons.org/licenses/by/4.0/).

1. Introduction

In the modern era of aerospace technology, significant advancements in lunar landers have been achieved through extensive research and development by various space agencies and private companies [1–3]. These landers typically rely on a descent stage equipped with propulsion systems to ensure precise and controlled landings on lunar or planetary surfaces [4–6]. Among the innovative developments in propulsion technology, liquid oxygen (LOX) and liquid methane (LCH4) have emerged as leading propellants due to their closely matched thermophysical properties and their potential for In Situ Resource Utilization (ISRU) on the Moon and Mars [7–14]. LOX-LCH4 engines are particularly valued for their high specific impulse, a key measure of rocket engine efficiency, which typically ranges between 300 and 340 s in vacuum conditions. This performance is comparable to the high-efficiency Liquid Hydrogen (LH2) systems but comes with reduced complexity in storage and handling requirements [15,16]. Unlike LH2, which demands extremely low cryogenic temperatures, both LOX and LCH4 can be stored at more manageable conditions, and LCH4 offers the additional benefit of cleaner combustion with fewer particulate emissions compared to traditional RP-1 kerosene-based fuels, resulting in a lower environmental footprint [17–19].

Despite these advantages, several challenges remain for the widespread adoption of LOX-LCH4 propulsion systems. One critical issue is thermal management. The cryogenic nature of LOX and the relatively milder storage requirements of LCH4 create significant thermal gradients, which can induce thermal stress and complicate engine and storage system design [20]. Moreover, achieving stable and efficient combustion with LOX-LCH4 is non-trivial due to the high energy density and rapid combustion rates of this propellant combination, necessitating advanced engineering solutions to ensure consistent performance across diverse operating conditions [21,22]. Factors such as combustion chamber geometry, nozzle design, and propellant mixing efficiency significantly influence the overall specific impulse and operational reliability of these engines [23]. Furthermore, the high costs and long timelines associated with engine development and rigorous testing can hinder the rapid adoption of LOX-LCH4 technology [24,25]. Addressing these challenges requires a multi-faceted approach, including extensive experimental validation under varied operating conditions and the integration of advanced digital engineering tools. For instance, the development of digital twins for LOX-LCH4 propulsion systems could enable detailed simulations and predictive analyses, helping optimize designs, enhance performance, and reduce development time and costs. Through such comprehensive efforts, LOX-LCH4 technology can overcome its current limitations and play a pivotal role in the future of space exploration.

A digital twin is a sophisticated model of a physical system represented in a digital environment, designed to replicate and predict real-life phenomena in real time [26–30]. This powerful tool enhances design and development processes by increasing accuracy, precision, and system integration, while reducing costs, risks, and the need for physical prototypes. In the aerospace industry, particularly in the development and optimization of liquid oxygen (LOX) and liquid methane (LCH4) propulsion systems, digital twins play a pivotal role. They enable real-time monitoring and control of propulsion systems, offering the ability to simulate, predict, and respond to system behavior under various operational conditions. This capability is essential for enhancing the performance, safety, and reliability of space missions. By identifying potential failures—such as malfunctions in LOX and LCH4 systems—before they occur, digital twins can significantly reduce downtime and prevent catastrophic failures during missions [31–33]. Furthermore, these digital models allow engineers to optimize fuel efficiency and thrust in real-time, adapting to changing conditions [34]. The use of digital twins also streamlines the design process, minimizing the need for costly physical prototypes and accelerating innovation through iterative modeling. This enables rapid identification of optimal system configurations [35]. Additionally, the integration of complex subsystems, such as turbo pumps and combustion chambers, is facilitated by digital twins, which helps mitigate the risk of unforeseen interactions that could lead to catastrophic failures [36]. While digital twins offer immense potential in improving the design, testing, and operational optimization of LOX and LCH4 propulsion systems, this field remains in development, requiring further modeling, testing, and validation to achieve high-fidelity simulations.

Inspired by the aforementioned research efforts, the Aerospace Center at UTEP is advancing the LOX-LCH4 propulsion system by developing a comprehensive understanding of the Centennial Restartable Oxygen Methane Engine (CROME), a 500-lbf, throttleable, bi-propellant engine designed for future lunar landers [37,38]. A key aspect of this research is the development of a digital twin for the CROME system. This involves developing several physics-based models—thermal, structural, flow, and combustion—which will be integrated and validated with real-world test data. In this study, the focus is on the digital modeling of the feed system, specifically fluid flow through critical components such as the propellant tank, feed system, and engine under varying operating conditions (P_{tank} = 33 psi

and $\dot{m}_{LCH4} = 0.9$ lbm/s and P_{tank} = 100 psi and $\dot{m}_{LCH4} = 0.9$ lbm/s). The overarching goal is to develop a robust digital twin that enhances thermal management, improves engine performance, and supports the advancement of cryogenic propellant technologies to meet lunar lander mission requirements.

2. Methodology

As mentioned in the Introduction, two test conditions were chosen to analyze the thermal and flow behavior in the CROME feed system: one at P_{tank} = 33 psi (227.5 kPa) and $\dot{m}_{LCH4} = 0.9$ lbm/s (0.4 kg/s), and another at P_{tank} = 100 psi (689.5 kPa) with the same mass flow rate. These pressures were selected based on preliminary findings showing changes in flow stability and pressure drop. For validation, an ESP model was used for the first condition and a VOF model for the second, supported by experimental data. The details of research methodology, including experiments, each model, meshing, boundary, and initial conditions, are provided below.

2.1. Experimental Test Setup

The CROME test skid consists of two primary sections: the feed line and the engine. During each cold flow test, the entire skid was monitored to ensure proper thermal management of the propellant. Below is a summary of the experimental test setup:

2.1.1. CROME

The Centennial Restartable Oxygen Methane Engine (CROME) (see Figure 1) is a pressure-fed, throttleable liquid oxygen and methane engine with a 4:1 throttle ratio, producing thrust from 500 to 125 lbf. Controlled via main engine valves, CROME is designed for upper stages requiring adjustable, low-thrust propulsion [38,39]. The current design is a heavy ground-test article featuring a bolt-on injector and chamber for inspection, 17 acoustic cavities to mitigate combustion instabilities, a side-mounted igniter, and dynamic/chamber pressure transducers for data collection during testing. The injector, engine chamber, and nozzle specifications and requirements are provided in Table 1.

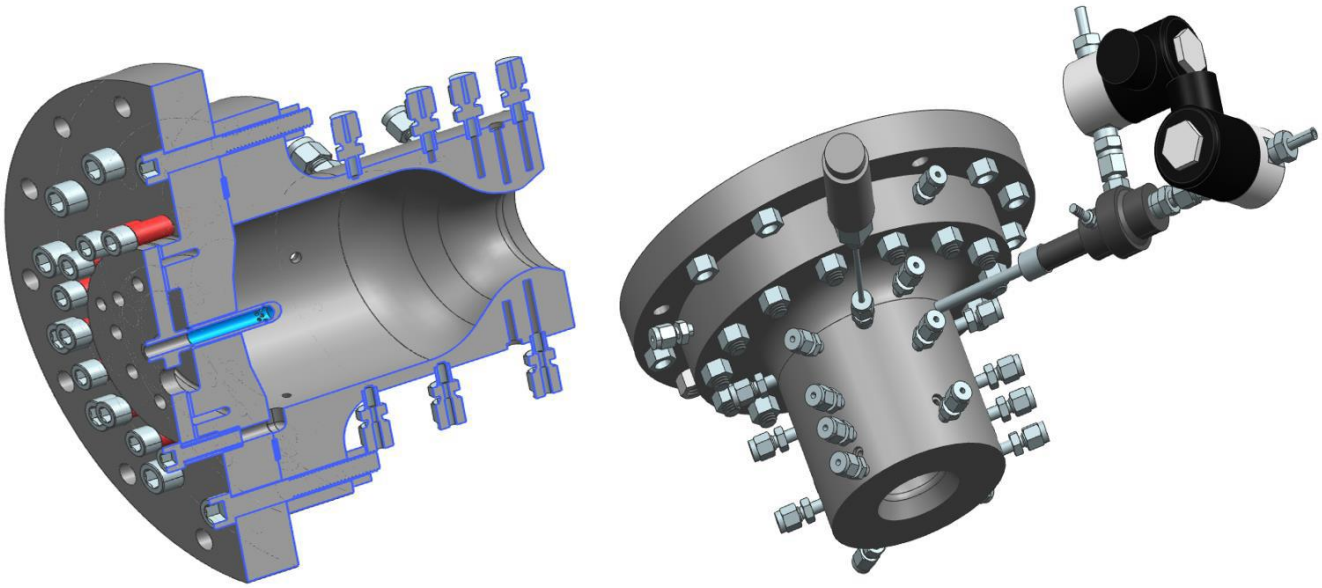


Figure 1. Isometric and cross-section rendering of CROME, with attached igniter torch [38].

Table 1. Injector, engine chamber, and nozzle derived requirements [38,40,41].

Requirements	Value
Thrust	500–125 lbf
Operation/Ambient Pressure	Steady State/12.8 psia
Propellants	LOX/LCH4
Max Tank Pressure	425 psig
Engine Mixture Ratio	2.7
Fuel Film Cooling (FFC)	30% of Incoming Fuel Flow
Engine Chamber Pressure (Pc)	235-70 psia
Component Materials	Chamber/Nozzle: Inconel 718 Injector Assembly: Inconel 625 Manifolds and Lines: SS 316
Nozzle Expansion Ratio (ε)	1.7

2.1.2. Feed System

The Centennial Restartable Oxygen-Methane Engine (CROME) Test Skid at UTEP's Tech 1 campus integrates a feed system to manage pressurized propellant flow and an engine to produce thrust (See Figures 2 and 3). The feed system includes LOX and LCH4 propellant tanks, which supply propellants through lines equipped with components such as pressure regulators, transducers, thermocouples, and cryogenic valves (manual and solenoid) (See Figure 2a). Throttle valves (Figure 2c), adjustable between 25% and 100% openings, enable precise control of mass flow rates to the engine, while orifices manage flow for fuel-film cooling (FFC). The FFC system, maintaining a 30% flow rate, effectively cools the engine walls (Figure 2b) across varying throttle conditions. This setup allows the engine to operate efficiently under diverse thrust requirements. For further technical details, see [38]. The details about the engine design, test facility, and engine testing campaign can be found elsewhere [38–41]. The schematic of the propellant tank, load cell, and close-up view of the engine chamber is provided in Appendix A, Section A, Figure A1.



Figure 2. *Cont.*

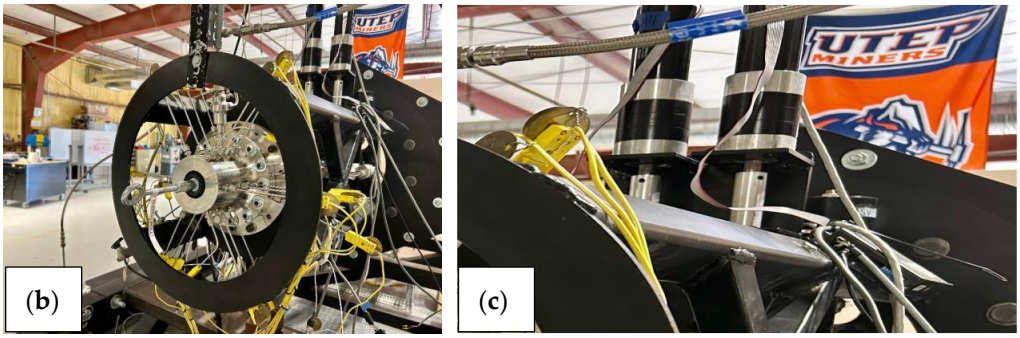


Figure 2. CROME test facility: (**a**) test skid with propellant tanks, feed lines, and engine; (**b**) engine module; and (**c**) throttle valves.



Figure 3. The master CAD showing all the major components of the CROME test setup [39].

2.1.3. Cold Flow Testing Strategies

Cold flow tests using liquid nitrogen (LN2) were performed to assess the feed lines' behavior under different tank pressures. These tests aimed to ensure the propellants retained their thermal properties and remained in the liquid phase before reaching the engine. They also validated instrumentation functionality, assessed sensor performance in cryogenic conditions, and provided preliminary data for CFD analysis. Observations included system responses, such as pressure, temperature, and mass flow rate variations, across components like tanks, regulators, solenoid valves, venturies, throttle valves, injector inlet, engine chamber, and nozzle.

The initial test matrix outlines the first phase of cold flow testing, focusing on validating the operability of both the test facility and the engine. Subsequent testing phases will aim to extend run durations, perform mixture ratio (MR) sweeps, and conduct active throttle evaluations. Tank pressure was determined by summing the estimated pressure drops across critical components, including valves, the engine manifold, the injector, and the required chamber pressure. These estimates, based on anticipated flow rates for hot-fire tests, will be confirmed during initial tests. Following the characterization of facility resistance for each propellant, the test matrix will be adjusted accordingly. A simplified version of the test matrix is presented in Table 2, with additional details on the shutdown (cut-off) sequence, and major instrumentation with their brand names, range and accuracy provided in Appendix A, Section B, Tables A1 and A2.

Table 2. Cold flow test matrix used to evaluate the propellant thermal properties across the CROME feed system.

Cold Flow Tests	Feed Line	Tank Pressure (psi)	Mass Flow Rate (lbm/s)	Expected Saturation Temperatures at The Engine Inlet (°F)
Test 1	LCH4	33	0.9	−309 to −312
Test 2		100		−283 to −285

To meet the future hot-fire test deadlines and ensure reliable data acquisition, understanding, maintaining, and upgrading testing instrumentation is critical. This involves the precise synchronization and operation of components such as pressure transducers, thermocouples, solenoid valves, and venturis, managed via LabVIEW using cRIO and cDAQ systems (see Figure 4). Cold flow testing plays a crucial role in optimizing data collection, improving safety, and facilitating hardware and software modifications. Data collected from the cold flow tests evaluate the propellant feed system and engine chamber responses. Troubleshooting focuses on harness wiring issues and ensuring sensor connections. Safety improvements include Velcro straps for harness organization, label maker tape for safer labeling, and an oxygen purge system to reduce cleaning needs. Software updates also addressed issues like shared solenoid valve channels.



Figure 4. Front (**left**) and back (**right**) of data and control racks [42].

The cold flow testing procedure consists of three sequential phases: the tank chilling test, the steady-state test, and the purge test. Data acquisition during each phase is facilitated by the Modular Instrumentation and Control Interface Trailer (MICIT) system, which operates using National Instruments' LabVIEW software and hardware (see Figure 4). The LabVIEW programming is based on a state machine logic and data enqueueing template, modified to enhance modularity and incorporate a Field Programmable Gate Array (FPGA)

for improved system reliability. Additional details about the MICIT system and its configuration are available in Appendix A (Section C, Figures A2–A4) and prior references [42–44]. Collected data are stored locally, exported from LabVIEW, and post-processed in MATLAB. The analysis primarily focuses on data from the steady-state phase, with findings presented in the results and discussion sections.

2.2. Models Used to Validate the Test Conditions

2.2.1. Eulerian Single-Phase (ESP) Model for the First Case (P_{tank} = 33 psi and $\dot{m}_{LCH4}$ = 0.9 $\frac{lbm}{s}$)

The team initially explored several computational models, including Mixture Multiphase (MMP), Eulerian Multiphase (EMP), Lagrangian Multiphase (LMP), and Eulerian Single-Phase (ESP). The ESP model was found to converge more easily and provide credible results, making it the choice for validating the first test condition. This model incorporated a detailed 3D system of the LOX and LCH4 lines, as well as the engine components. The ESP model, which evaluates flow without phase terms (100% LN2), utilizes the RANS equations [45–47] to assess coupled flow, ensuring more stable simulations and facilitating adjustments to solver relaxation factors for convergence. Incorporating the k-ε turbulence model and segregated temperature for fluid temperature gradients further enhanced accuracy, allowing precise simulations of temperature and pressure at various upstream and downstream points. Figure 5 and Tables 3 and 4 detail the 3D CAD, mesh settings, and initial/boundary conditions.

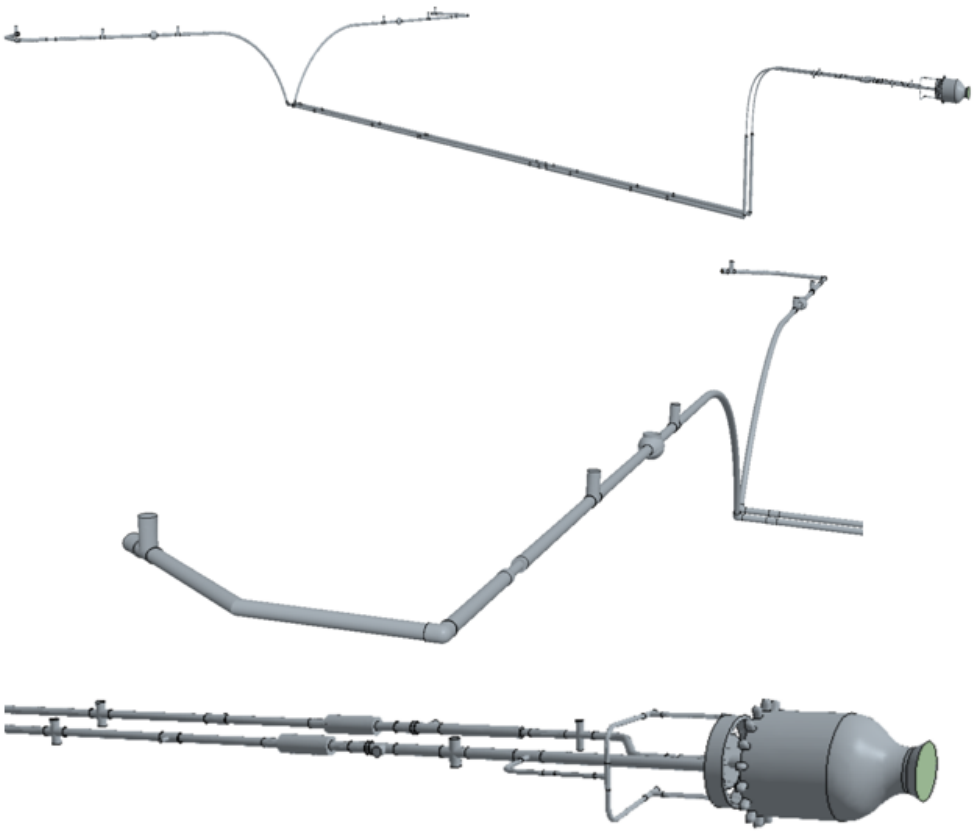


Figure 5. 3D CAD used in the ESP model: overall test skid CAD (**top**), feedline CAD (**middle**), and injector and engine CAD (**bottom**).

Table 3. Mesh and model inputs parameters for ESP simulation.

Categories	Parameters Used in ESP Simulation

Mesh Settings	• Base size = 0.1 m
	• Prism Layer Characteristics:
	  ○ # of Prism layers = 7
	  ○ Prism layer stretching = 1.1
	  ○ Volume growth rate = 1.2

Models	• Turbulence: k-ω • Reynolds Averaged Navier–Stokes (RANS) • Segregated Flow: Segregated Multiphase Temperature • Gravity and Steady • Liquid and Coupled Flow

Table 4. Boundary and initial conditions used in the ESP model.

Initial Conditions	• P_{tank} = 33 psi and $\dot{m_{LCH4}}$= 0.9 $\frac{lbm}{s}$

Regional Boundary Conditions	• Inlet: Mass flow inlet
	  ○ Mass flow inlet—Initial condition driven
	• Outlet: Outlet type
	• Walls, Venturi Segments: Wall type
	  ○ No-slip and Rough Wall
	  ○ Convection (multi-layer resistance)
	• Solenoid Valve, Throttle Valve Segments: Wall type, rough
	  ○ No-slip and Rough Wall
	  ○ Convection (Constant Thermal Resistance)

2.2.2. Volume of Fluid (VOF) Model for the Second Test Condition (P_{tank} = 100 psi and $\dot{m_{LCH4}}$ = 0.9 $\frac{lbm}{s}$)

It is important to note that the CROME feed system's propellant tank is designed to withstand a maximum pressure of 400 psi, with additional details on the system and testing approach provided in reference [38]. In the second cold flow test, a tank pressure of 100 psi was applied. During this test, significant boil-off phase change phenomena were observed throughout the feed system, necessitating the identification of a model, other than the ESP, capable of resolving the boil-off event and accommodating the liquid–gas volume fractions. To validate the second cold flow test data, the Volume of Fluid (VOF) model was selected. To account for heat transfer through conduction and convection to the atmosphere, boundary conditions were applied in place of solid components, minimizing computational costs and simulation time. Figure 6 illustrates the CAD model used for the simulation grid. The VOF model was chosen for its ability to simulate the interface between liquid and gaseous nitrogen phases [48–53], using Equations (1) and (2) to distinguish between the two phases.

$$\sum_{i=1}^{N} \alpha_i = 1, \quad (1)$$

$$\alpha_i = \frac{V_i}{V}, \quad (2)$$

where V_i is the volume fraction of the i phase, V is the total volume, and α_i is the volume fraction of the respective phase. This term is integrated into the fluid properties, which are then applied to solve the Reynolds Averaged Navier–Stokes (RANS) equations [45–47]. Along with the Volume of Fluid (VOF) method, Segregated Multiphase Temperature and k-ε

turbulence models for both gaseous and liquid phases are employed to ensure compatibility. Grid settings and models used in the simulation are listed in Table 5, with further settings and results discussed in the results section. Multiple simulation cases were developed, but only the best case is presented, based on the CFD analysis and test results. Boundary and initial conditions for the simulation are provided in Table 6.

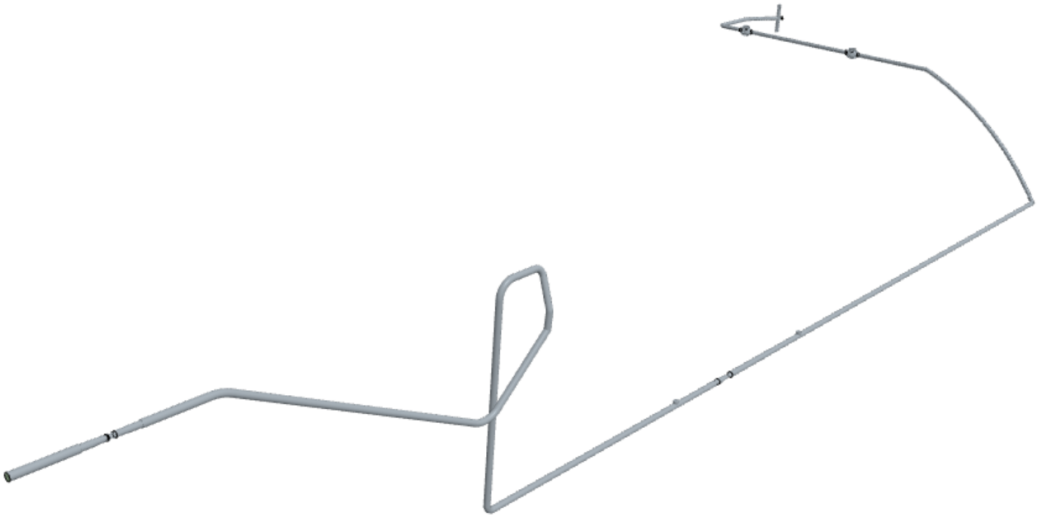


Figure 6. Simplified geometry CAD model for the LCH4 line.

Table 5. Mesh and model inputs for the VOF multiphase simulation.

Categories	Parameters

Mesh Settings	• Base size = 0.005 m
	• Prism Layer Characteristics:
	  ○ # of Prism layers = 5
	  ○ Prism layer stretching = 1.1
	  ○ Volume growth rate = 1.2
	• Custom controls:
	  ○ Target and min. surface sizes: 5% and 1%, respectively

Models	• Turbulence Model: k-ω
	• Multiphase Model: VOF
	  ○ LN2: Polynomial Density
	  ○ GN2: Ideal Gas
	• Multiphase Interaction
	  ○ VOF Interaction
	  ○ Evaporation/Condensation
	  ○ Multiphase Material
	• Reynolds Averaged Navier–Stokes (RANS)
	• Segregated Flow: Segregated Multiphase Temperature
	• Gravity and Steady

Table 6. Initial and boundary conditions used in the VOF model.

Initial Conditions	• P = 100 psi, T = −282.76 °F • Volume Fraction: Liquid = 1.0; Gas = 0.0

Regional Boundary Conditions	• Inlet: Mass flow inlet
	  ○ Mass flow inlet = 0.9 $\frac{lbm}{s}$
	• Outlet: Outlet type
	• Walls, Venturi segments: Wall type
	  ○ No-slip
	  ○ Convection (multi-layer resistance)
	  ○ Rough walls
	• Solenoid valve, Throttle Valve segments: Wall type
	  ○ No-slip
	  ○ Convection (Constant Thermal Resistance)
	  ○ Rough walls

3. Results and Discussion

The authors conducted two cold flow tests to evaluate the thermal and flow properties of the propellant system and ensure stable liquid-phase delivery at the injector inlet for future tests. The first test, conducted at 33 psi, confirms the system's ability to perform well under lower-pressure conditions. A second test was conducted at 100 psi tank pressure, revealing the need for system improvements to handle higher pressures safely. High-accuracy computational models validated the tests, with different modeling approaches (ESP and VOF) used for each case. The ESP model, validated at 33 psi, is designed to operate effectively within a pressure range of 0–400 psi. It has demonstrated accuracy in predicting critical thermo-fluid properties, such as pressure drops and temperature profiles, throughout this range. The same holds for the VOF model. However, this paper includes validation at only 33 and 100 psi, as experiments at other pressures are still ongoing. A detailed journal paper covering a broader range of pressures and digital twin validations is planned for later this year. The focus of this paper remained on thermal management of the methane line, excluding the LOX line. The experimental and CFD results are presented below:

3.1. Experimental Observation

The temperatures and pressures from the first and second cold flow tests are provided in Figures 7–9 and Figures 10–12, respectively. The data were recorded at a 15 s auto sequence through the central control station. Data were collected throughout the auto sequences, including tank chilling, feed line chilling, engine chilling, and purge steps. For each test, approximately 339,000 to 340,010 data were recorded, and the team extracted steady-state data for improved statistical analysis. In addition, the statistical data for critical thermo-fluid properties are listed in Table 7.

Table 7. Statistical data of the critical thermo-fluid properties observed during the cold flow tests.

Parameters/Categories	First Test	Second Test
Sample Data Set	339,000	340,010
Venturi Mass Flow Rate (lbm/s)	0.833 to 0.906 Avg. = 0.869; Std Dev = 0.0048	0.851 to 1.08 Avg. = 0.965; Std Dev = 0.0047
Tank Surface Temperature (°F)	−300.4 to −298.7 Avg. = −299.5; Std Dev = 0.251	−298.1 to −279.2 Avg. = −288.6; Std Dev = 0.230
Tank Pressure (psi)	33.1 to 33.6 Avg. = 33.3; Std Dev = 0.30	100.3 to 101.6 Avg. = 100.9; Std Dev = 0.31

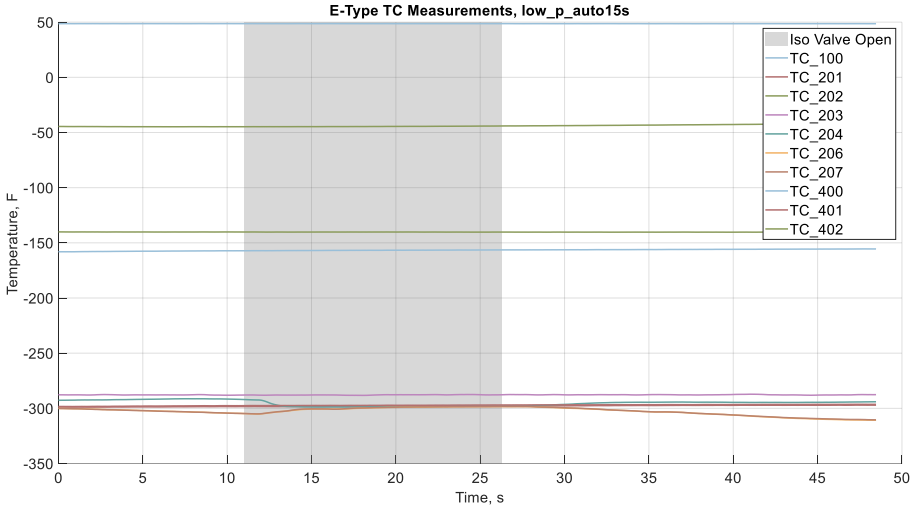


Figure 7. Temperature observed across the feed line and engine chamber during the first cold flow test (P_{tank} = 33 psi).

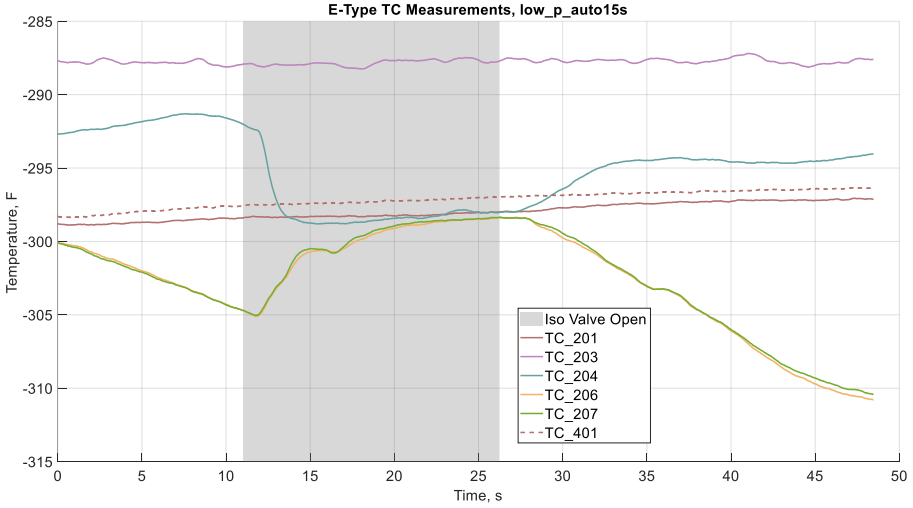


Figure 8. Temperatures of critical sensors (zoomed in view of the previous figure) observed across the feed line and engine chamber during the first cold flow test (P_{tank} = 33 psi).

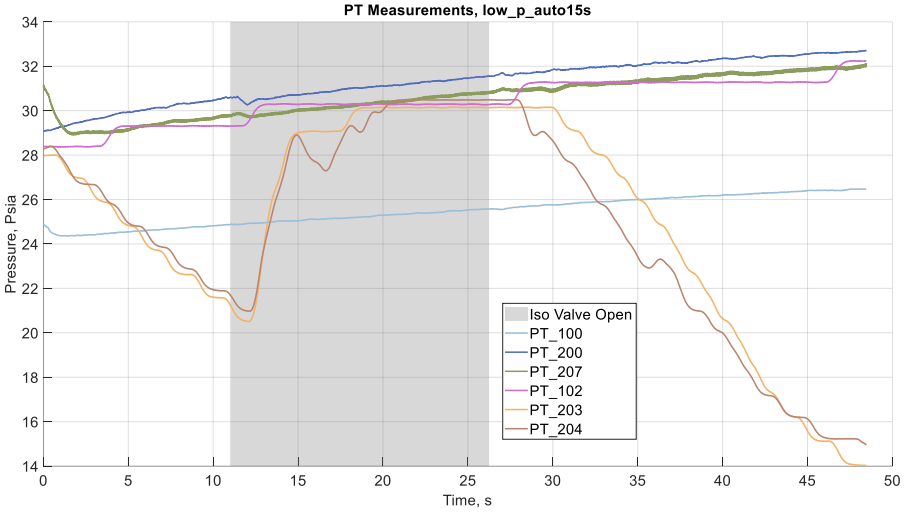


Figure 9. Pressures observed across the feed line and engine chamber during the first cold flow test (P_{tank} = 33 psi).

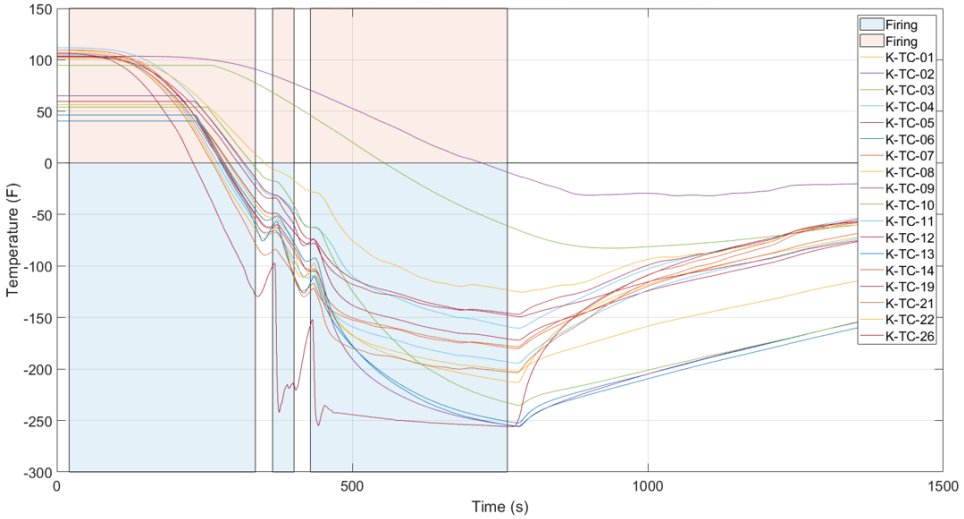


Figure 10. Temperature observed across the feed line and engine chamber during the second cold flow test (P_{tank} = 100 psi).

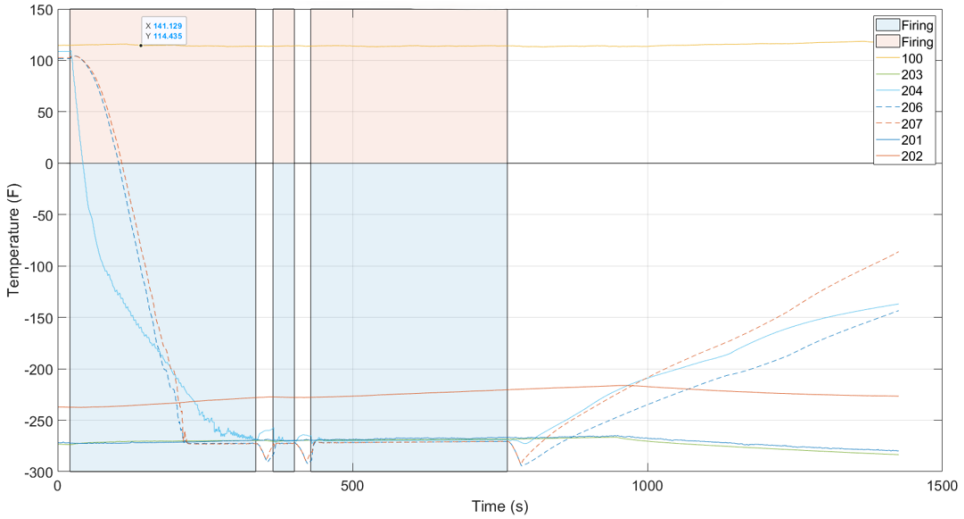


Figure 11. Temperatures of critical sensors (zoomed in view of the previous figure) observed across the feed line and engine chamber during the second cold flow test (P_{tank} = 100 psi).

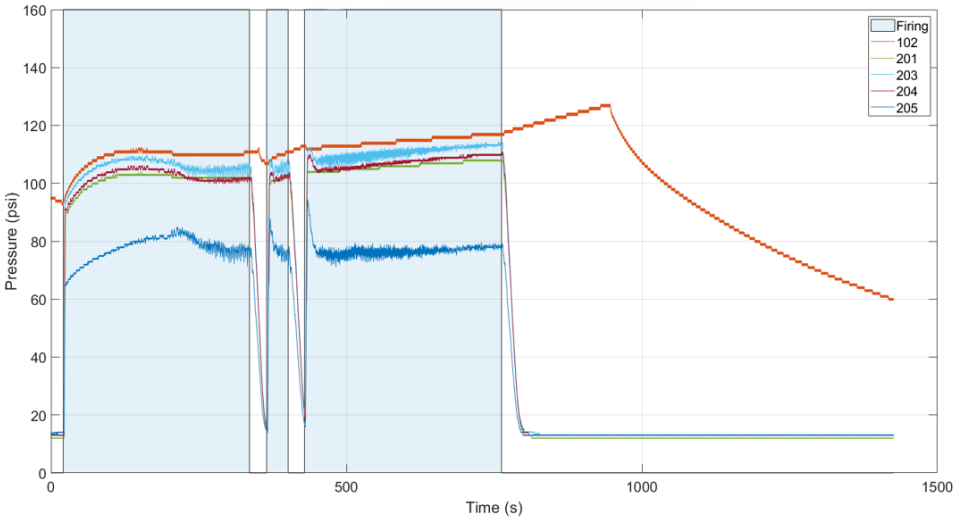


Figure 12. Pressures of critical sensors (zoomed in view of the previous figure) observed across the feed line and engine chamber during the second cold flow test (P_{tank} = 100 psi).

3.2. Performance Validation of CROME Feed System

3.2.1. General Convergence Criteria for ESP and VOF Models

The authors considered a general convergence criterion of 1×10^{-3} for residuals in simulations using the ESP and VOF models, focusing on continuity and energy residuals. The ESP method was run for 3000 iterations, while the VOF method completed 1375 iterations. In both cases, energy residuals fell below 1×10^{-3}, confirming full convergence. However, continuity residuals exceeded 1×10^{-2} for the ESP method and 1×10^{-1} for the VOF method. Despite not meeting the 1×10^{-3} threshold for continuity, the authors observed very negligible variations in pressure and temperature across the domain for a long time, indicating further iterations would not significantly affect the results. Simulations were concluded at this point to optimize storage and computational efficiency. Figures 13 and 14 illustrate the residuals for the ESP and VOF methods, respectively.

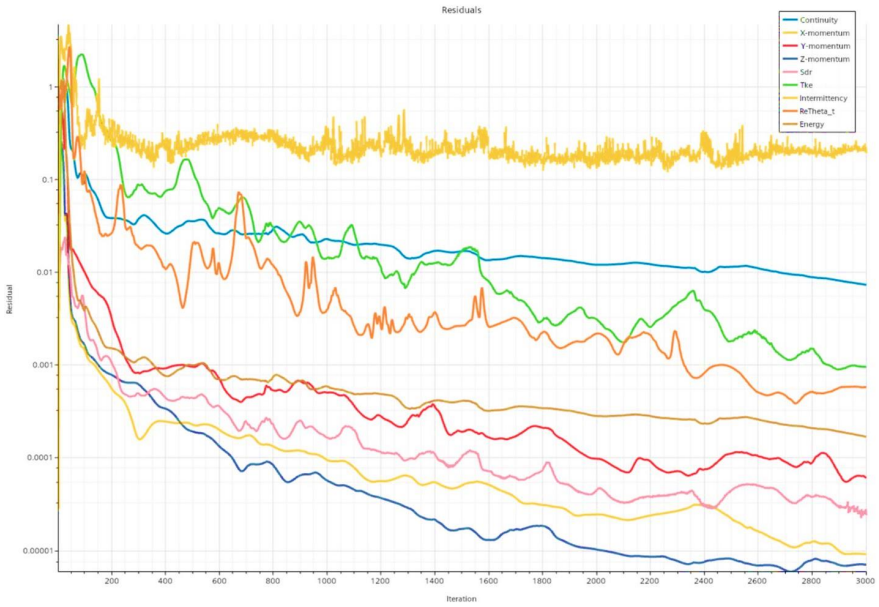


Figure 13. Simulation residual plot for the ESP method.



Figure 14. Simulation residual plot for the VOF method.

3.2.2. Feed System Behavior Using ESP for the First Case

The ESP monitors LN2 pressure and temperature changes along the LCH4 feed line and engine. Static pressure remains steady between 14.6 and 16 psi (see Figures 15 and 16), with maximum experimental pressures of 17.1 psi in the LCH4 line and 17.5 psi in the engine, showing deviations of 6.4% and 8.6% (Table 8), respectively. CFD simulations align closely with experimental total pressures, showing a 6.4% deviation at the LCH4 inlet (31 psi experimental vs. 33 psi CFD) and similar values (~29.6 psi) at the engine inlet. These findings validate the accuracy of the Eulerian Single-Phase model for LN2 cold flow simulations.

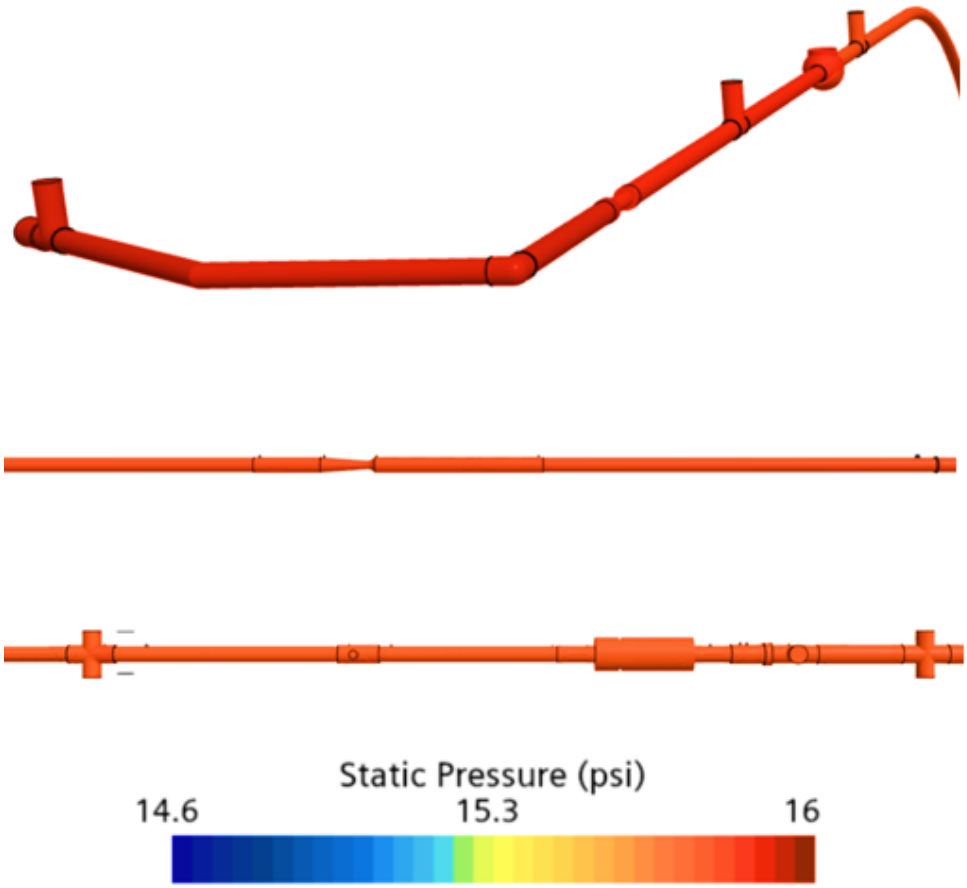


Figure 15. Static pressure contours for the LCH4 line.

Table 8. Properties across feed line and engine for 1st test (P_{tank} = 33 psi).

Parameters	Experimental	CFD	|*Deviation*(%)|
Fixed Initial Conditions	$P_{tank} = 33.0 \pm 2.0$ psi $\dot{m}_{LCH4} = 0.9 \pm 0.075$ $\frac{lbm}{s}$	$P_{tank} = 33.0$ psi $\dot{m}_{LCH4} = 0.9$ $\frac{lbm}{s}$	
$P_{LCH4\ Inlet}$	31.0 ± 2.0 psi	33.0 psi	6.4
$T_{LCH4\ Inlet}$	-287.3 ± 1.5 °F	−299 °F	4.1
$P_{Engine\ Inlet}$	29.6 ± 2.0 psi	29.6 psi	--
$T_{Engine\ Inlet}$	-300.0 ± 2.25 °F	−294.0 °F	2.0
$P_{S(\max)LCH4\ Line}$	17.1 ± 2.0 psi	16.0 psi	6.4
$P_{S(max)Engine}$	17.5 ± 2.0 psi	16.0 psi	8.6%

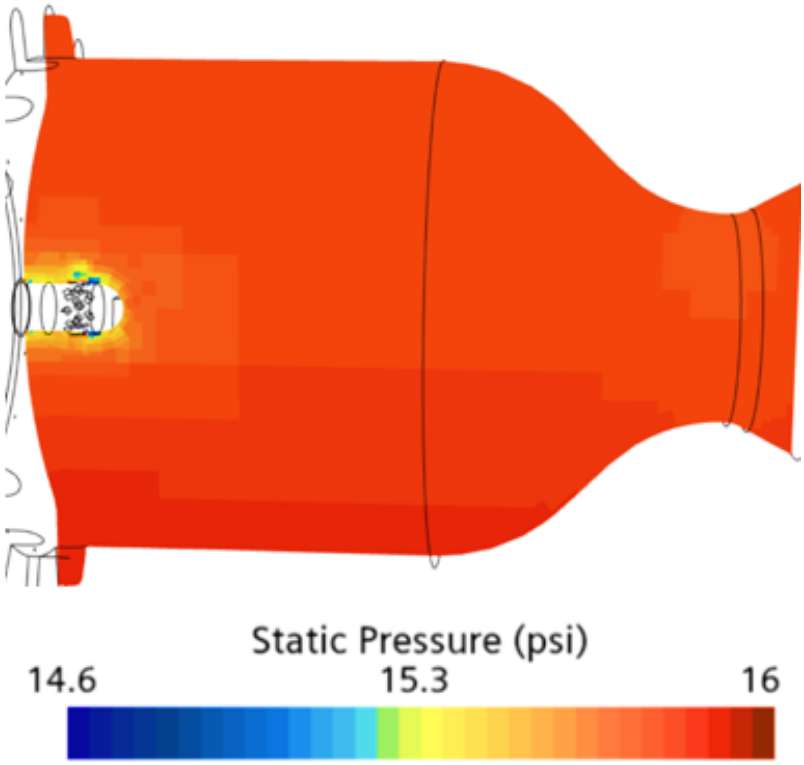


Figure 16. Static pressure contours for the engine.

LN2 temperatures, however, vary significantly from the feed line to the engine chamber. In the feed line, temperatures range from −323 °F to −250 °F, while in the engine, they vary from −300 °F to −211 °F (Figures 17 and 18). This indicates a transition from liquid to vapor phase as LN2 passes through solenoid valves and injection points. The temperatures of −299 °F and −294 °F were observed at the LCH4 line inlet (propellant tank outlet) and engine inlet, respectively, which align closely with experimental measurements of −287.3 °F and −300 °F at the same points, showing deviations of 4.1% and 2.0% (Table 8).

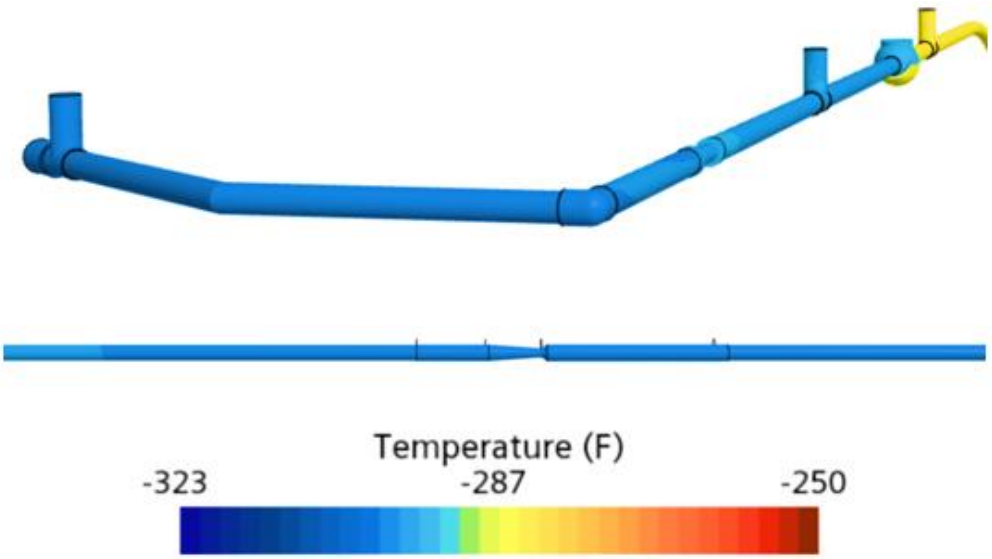


Figure 17. Temperature contours for the LCH4 line.

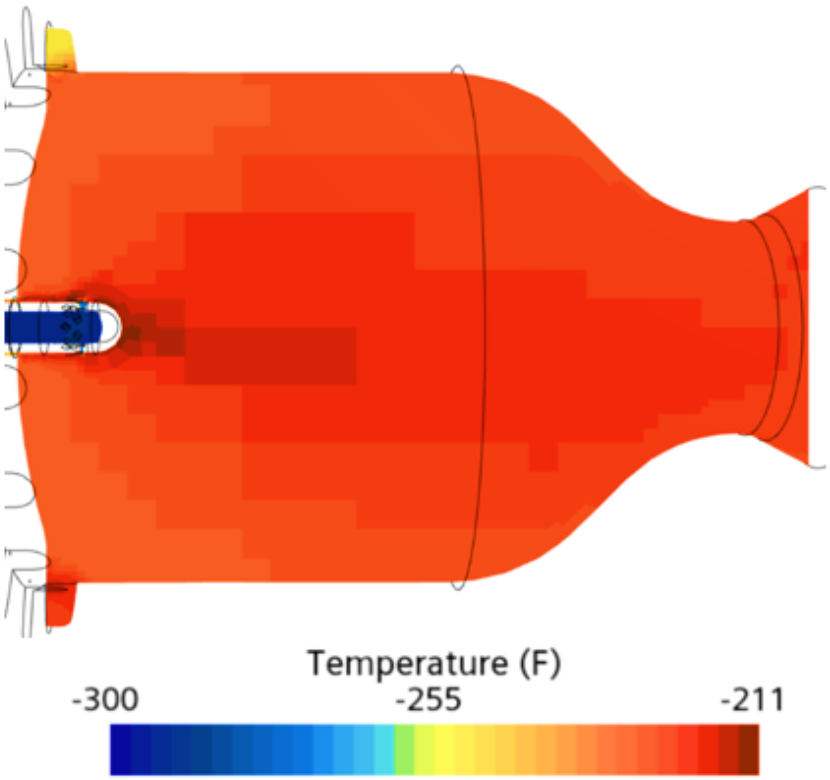


Figure 18. Temperature contours for the engine.

3.2.3. Feed System Behavior Using VOF for the 2nd Case

In the second cold flow test, a pressure change of +3.0 psi was recorded across the LCH4 feed line. Using a Volume of Fluid (VOF) model with an initial assumption of 100% LN2 and 0% GN2, a pressure change of −26.3 psi was predicted, which significantly differed from the observed result. The team concluded that the propellant underwent significant boil-off [38,54,55], resulting in both liquid and gaseous phases. To refine the VOF model, eight cases were considered, varying from 100% LN2 to 100% GN2 (Table 9). At 50% LN2 and 50% GN2 mixture conditions, the pressure change was −11.3 psi. At 100% GN2, the pressure change increased to +3.1 psi (Figures 19 and 20), closely matching the test data (+3.0 psi) with a 3.3% error margin. The deviation between the CFD results and experimental data highlights further refinement of the CFD model. It also indicates the system's sensitivity to high-pressure test conditions and external factors, such as ambient conditions. This highlights the need for better insulation, recalibration of the pressure transducer (PT) and thermocouple (TC), the addition of more PTs and TCs for improved phase change detection, and changes to the tank filling, chilling, and venting processes.

Table 9. Pressure changes between CFD and experimental tests.

Cases	Mixture Fractions	ΔP_{CFD}	$\Delta P_{Experimental}$
1	100% LN2	26.3 psi (Drop)	
2	80% LN2, 20% GN2	18.2 psi (Drop)	
3	50% LN2, 50% GN2	11.3 psi (Drop)	
4	45% LN2, 55% GN2	7.2 psi (Drop)	3 psi (~20.7 kPa) (Rise)
5	10% LN2, 90% GN2	0.2 psi (Drop)	
6	5% LN2, 95% GN2	0.44 psi (Rise)	
7	2% LN2, 98% GN2	3.3 psi (Rise)	
8	100% GN2	3.1 psi (~21.4 kPa) (Rise)	

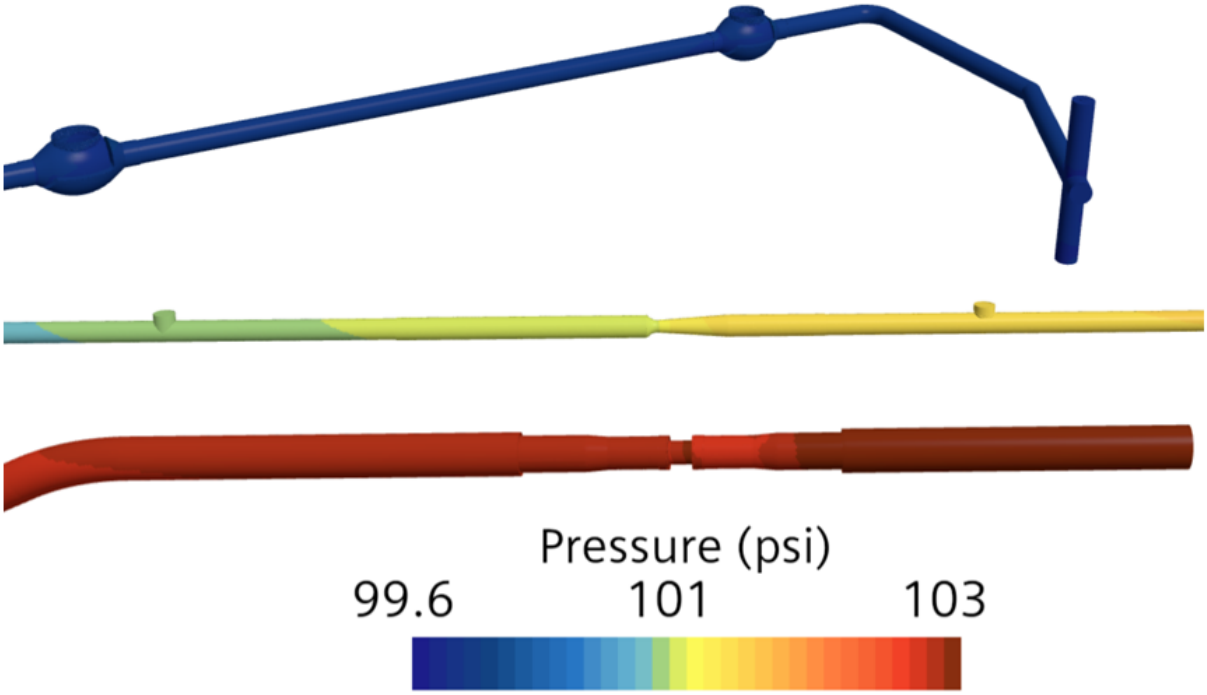


Figure 19. Pressure contours: inlet segment (**top**), Venturi flowmeter (**middle**), and throttle valve segment and model outlet (**bottom**).

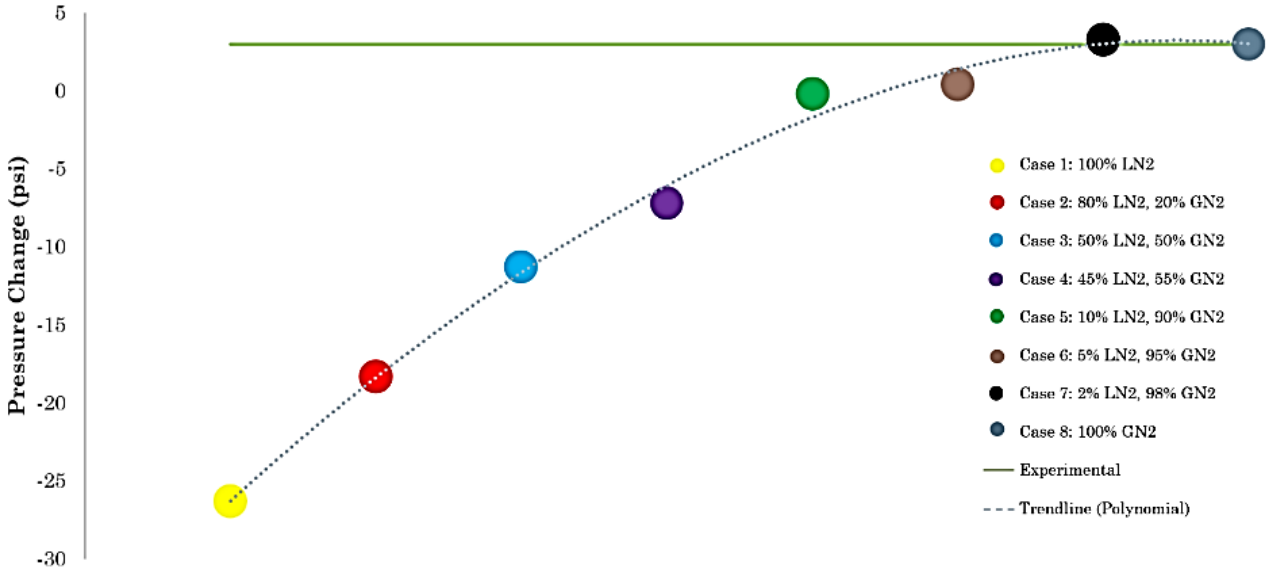


Figure 20. CFD (VOF) vs. experimental ΔP comparison graph.

The experimental pressure change data were also validated using a simplified VOF method, demonstrating that the model was appropriately calibrated to represent the thermal behavior of the feed line. While several properties were analyzed, the focus was on the propellant's temperature change, as monitoring both temperature and pressure was essential for managing the propellant's phase transitions in the feed line. The LN2 temperature ranged from −236 °F to −300 °F (Figure 21), fluctuating around the saturation temperature of −283 °F (at 100 psi), indicating the occurrence of phase transitions rather than a stable liquid state.

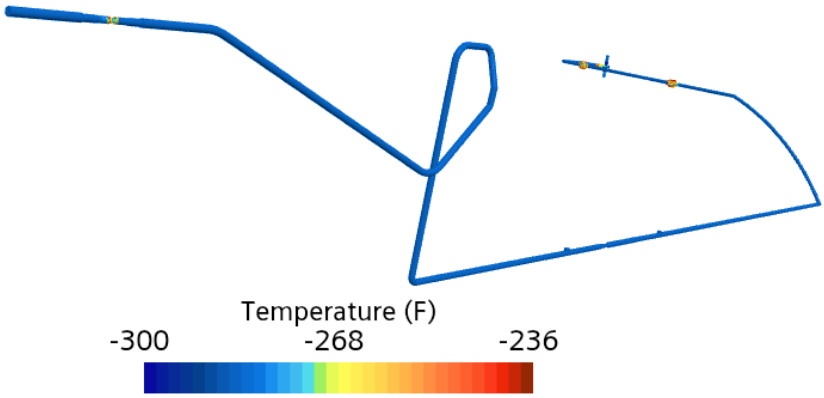


Figure 21. Change in temperature at P_{tank} = 100 psi when LN2 flows across the feedline.

The authors emphasize improving model accuracy and reliability by optimizing meshing, solver settings, discretization, y+ values, relaxation factors, and the Courant number. The authors also highlight the need for training and calibrating models across diverse conditions and validating them with experimental data. The authors are developing hardware models for flow, thermal, structural, and combustion systems, integrating them into a CROME digital twin. This twin will synchronize with test and simulation data for calibration and validation, incorporating uncertainty quantification, propagation, and fidelity assessment to improve model reliability within a digital engineering framework.

4. Conclusions

This paper examines the thermal management of the LOX-LCH4 propulsion system, focusing on the thermo-fluid behavior of the feedlines. The primary objective is to maintain the propellant in the liquid phase. Additionally, it aims to contribute to the ultimate development of a digital twin for the CROME to enhance predictive capabilities, scalability, and early failure detection. Two test operating conditions were considered to evaluate the system's sensitivity and thermal-flow properties. In the first test (P_{tank} = 33 psi, $\dot{m}_{LCH4} = 0.9$lbm/s), Eulerian Single-Phase (ESP) model was found to be the most accurate model for validation of experimental data. The static pressure from ESP is found to be stable, ranging from 14.6 to 16 psi, with experimental maximum pressures of 17.1 psi in the LCH4 line and 17.5 psi in the engine, showing less than a 1.5 psi (~8.5%) difference between experiments and CFD. LN2 temperatures vary significantly from −323 °F to −250 °F in the feed line and from −300 °F to −211 °F in the engine, indicating a phase change from liquid to vapor. The model predicted maximum temperatures of −299 °F and −294 °F at the LCH4 line and engine inlets, closely matching experimental maximum values of −287.3 °F and −300 °F, with deviations of 4.1% and 2.0%, respectively. The pressure changes also correlated well, with ~6.4% and ~8.6% deviations in the LCH4 line and engine, demonstrating good agreement between experimental and computational results.

From the second test (P_{tank} = 100 psi, $\dot{m}_{LCH4} = 0.9$lbm/s), an experimental pressure change of +3 psi was noted between the tank inlet and the engine chamber inlet. The VOF model with a simplified geometry and 100% LN2 simulation showed a −26.3 psi pressure change, indicating phase changes with boil-off occurring before the propellant reached the engine. For that, within the VOF model, various volume fractions have been explored, revealing that a mixture of 50% LN2 and 50% GN2 resulted in a −11.3 psi pressure change, while 2% LN2 and 98% GN2 showed a +3.3 psi pressure rise. The closest match to experimental data (+3 psi) was observed with 100% GN2, showing a +3.1 psi rise with only a 3.3% error. The study highlighted the importance of improved control over valves, regulators, sensors, and orifices to prevent heat gain and maintain proper saturation temperature and pressure. It also stressed the need for better insulation and

thermal management of the propellant tank. These digital models aid in developing the CROME feed system's digital twin and optimizing cryogenic propellant management.

5. Future Work

Future work will focus on enhancing the accuracy of the CROME feed system's digital twin (DT) by refining meshing, solver settings, and model discretization, alongside adjustments to relaxation values, y+ values, and the Courant number. The research will integrate flow, thermal, structural, and combustion models into a unified "digital engineering platform" to synchronize test and digital data for communication, calibration, and validation. This platform will enable uncertainty quantification, performance optimization, and lifecycle analysis for real-world engine testing and operations.

Author Contributions: Conceptualization, A.C. and M.A.H.; methodology, I.H., S.O. and M.A.H.; software, A.C., M.A.H., I.H. and S.O.; validation, M.A.H., I.H. and S.O.; formal analysis, M.A.H., I.H. and S.O.; investigation, M.A.H., I.H. and S.O.; resources, A.C. and M.A.H.; data curation, M.A.H., I.H. and S.O.; writing—original draft preparation, M.A.H., I.H. and S.O.; writing—review and editing, M.A.H. and S.O.; visualization, I.H. and S.O.; supervision, A.C. and M.A.H.; project administration, A.C.; funding acquisition, A.C. All authors have read and agreed to the published version of the manuscript.

Funding: This material is based on research sponsored by the Air Force Research Laboratory under agreement number FA8650-20-2-5700. The U.S. government is authorized to reproduce and distribute reprints for governmental purposes notwithstanding any copyright notation thereon.

Data Availability Statement: The data presented in this study are available on request from the corresponding author. The data are not publicly available due to the ITAR and/or agency's policies.

Acknowledgments: The authors would like to acknowledge the UTEP Aerospace Center for the tools and guidance that made this analysis possible and the rest of the Aerospace Center lander team for their knowledge and support. The authors extend their gratitude to the project mentors and faculty supervisors for their invaluable support in developing this analysis. They also thank Pilar Gonzales, a project engineer, for her steadfast assistance with the cold flow test. Additionally, they acknowledge the prior contributions of researchers Manuel Jesus Herrera, Raymundo Mendivil Rojo, and Zachary Welsh, whose efforts laid the foundation for the current research.

Conflicts of Interest: The authors declare no conflict of interest.

Disclaimer: The views and conclusions contained herein are those of the authors and should not be interpreted as necessarily representing the official policies or endorsements, either expressed or implied, of the Air Force Research Laboratory or the U.S. Government.

Nomenclature

CROME	Centennial Restartable Oxygen Methane Engine
GFSSP	Generalized fluid system simulation program
GN2	Gaseous Nitrogen
LCH4	Liquid Methane
LN2	Liquid Nitrogen
LOX	Liquid oxygen
lbf	Pound force
ΔP	Pressure change
RANS	Reynolds Averaged Navier–Stokes
ΔT	Temperature change
VOF	Volume of Fluid
ESP	Eulerian Single-Phase

Appendix A

A. Test Setup:



Figure A1. Propellant tank, load cell and close-up view of the engine chamber (from left to right).

B. Cold Flow Test:

Table A1. The cut-off sequence used during the cold flow test.

Cut-Off Shutdown Sequence	
Time (sec)	**Event**
0	TV-200, TV-300, SV-201, and SV-301 are **CLOSED**, Propellant Flow is Stopped
0.5	SV-202, SV-203, SV-102, and SV-103 are **OPENED**, Bleed Lines and Propellant Tank Lines are **OPENED**
1	SV-104, SV-105, SV-106 are **OPENED**, Run-line and Engine Purges are **OPENED**
31	SV-104, SV-105, SV-106 are **CLOSED**, Run-line and Engine Purges are **CLOSED**
32	TV-200 and TV-300 are fully **OPENED**, Main Engine Valves **OPENED**
33	SV-202 and SV-203 are **CLOSED**, Bleed Lines are **CLOSED**
34	SV-105 and SV-106 are **OPENED**, Run-line Purge through Main Engine Valves are **OPENED**
44	SV-105 and SV-106 are **CLOSED**, Run-line Purge through Main Engine Valves are **CLOSED**
45	TV-200 and TV-300 are fully **CLOSED**, Main Engine Valves **CLOSED**
46	SV-107 and SV-108 are **OPENED**, Igniter Purge is **OPENED**
56	SV-107 and SV-108 are **CLOSED**, Igniter Purge is **CLOSED**
	End of Cut-off Shutdown Sequence

Table A2. List of major components with their brand names, range and accuracy.

Components Names	**Vendor**	**Range**	**Accuracy**	**Types**
Pressure Transducer	Omega or Generant	0–1000 psig	0.1% to 0.25%	Cryo or Static
Thermocouples	Omega	32 to 1652 °F (E-Type) 32 to 2282 °F (K-Type)	±1.7 °C (E-Type) ±2.2 °C (K-Type)	E-Type or K-Type (Grounded, Ungrounded, or Exposed)
Solenoid Valves	Gems Sensors & Controls or Clark Cooper Peterpaul	375–1500 psia	±1% to 10%	Cryo
Venturi	Lord	0–300 psid	0.25% FSO ±1% of C_d	Cryo

C. Data Acquisition and Control System:



Figure A2. The MICIT used for sensing signal and data acquisition.

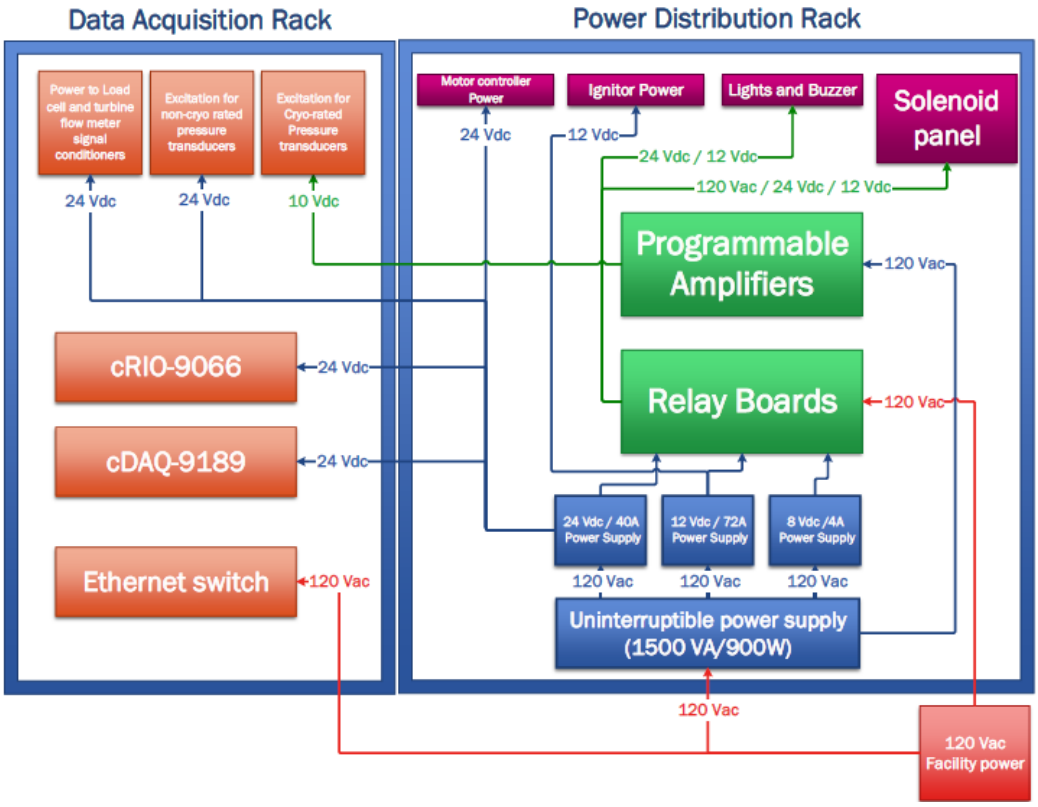


Figure A3. Diagram that shows how the different components in MICIT are powered [44].

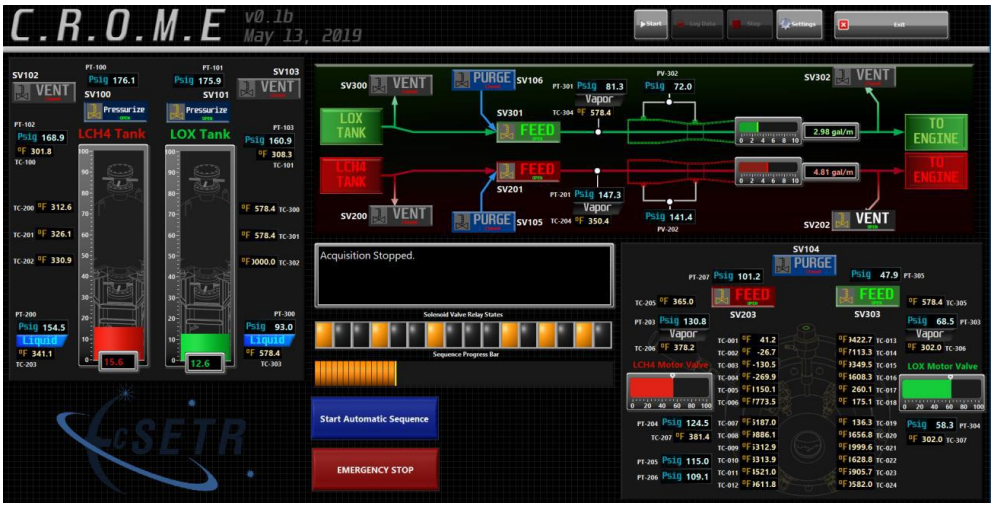


Figure A4. Main.vi front panel for CROME [44].

References

1. Hao, Z.; Xintong, L.; Yuanjun, Z.; Yang, L.; Hui, T.; Guobiao, C. Trajectory/propulsion integrated design optimization of the manned lunar lander propelled by hybrid rocket motors using analytical target cascading. *Acta Astronaut.* **2024**, *222*, 375–390.
2. Shi, T.; Yang, Y.; Zhang, Z.; Liu, C.; Liu, C.; Ma, D. Soft-landing dynamics of a type of four-legged space lander. *Aerosp. Sci. Technol.* **2024**, *150*, 109217. [CrossRef]
3. Cohen, B.A.; Chavers, D.G.; Ballard, B.W. NASA's robotic lunar lander development project. *Acta Astronaut.* **2012**, *79*, 221–240. [CrossRef]
4. Evans, M.E.; Graham, L.D. A flexible lunar architecture for exploration (FLARE) supporting NASA's Artemis program. *Acta Astronaut.* **2020**, *177*, 351–372. [CrossRef] [PubMed]
5. Pontani, M.; Celani, F.; Carletta, S. Lunar descent and landing via two-phase explicit guidance and pulse-modulated reduced-attitude control. *Acta Astronaut.* **2023**, *212*, 672–685. [CrossRef]
6. Braun, M.; Gollins, N.; Trivino, V.; Hosseini, S.; Schonenborg, R.; Landgraf, M. Human lunar return: An analysis of human lunar exploration scenarios within the upcoming decade. *Acta Astronaut.* **2020**, *177*, 737–748. [CrossRef]
7. Spedding, C.P.; Lim, S.; Nuttall, W.J. ISRU technology deployment at a lunar outpost in 2040: A Delphi survey. *Acta Astronaut.* **2021**, *181*, 316–324. [CrossRef]
8. Bennett, N.J.; Ellender, D.; Dempster, A.G. Commercial viability of lunar in-situ resource utilization (ISRU). *Planet. Space Sci.* **2020**, *182*, 104842. [CrossRef]
9. Palos, M.F.; Serra, P.; Fereres, S.; Stephenson, K.; González-Cinca, R. Lunar ISRU energy storage and electricity generation. *Acta Astronaut.* **2020**, *170*, 412–420. [CrossRef]
10. Reid, E.; Iles, P.; Muise, J.; Cristello, N.; Jones, B.; Faragalli, M.; Visscher, P.; Boucher, D.; Simard-Bilodeau, V.; Apostolopoulos, D.; et al. The Artemis Jr. rover: Mobility platform for lunar ISRU mission simulation. *Adv. Space Res.* **2015**, *55*, 2472–2483. [CrossRef]
11. Guerrero-Gonzalez, F.J.; Zabel, P. System analysis of an ISRU production plant: Extraction of metals and oxygen from lunar regolith. *Acta Astronaut.* **2023**, *203*, 187–201. [CrossRef]
12. Hoffman, J.A.; Hinterman, E.R.; Hecht, M.H.; Rapp, D.; Hartvigsen, J.J. 18 Months of MOXIE (Mars oxygen ISRU experiment) operations on the surface of Mars-Preparing for human Mars exploration. *Acta Astronaut.* **2023**, *210*, 547–553. [CrossRef]
13. Anand, M.; Crawford, I.A.; Balat-Pichelin, M.; Abanades, S.; Van Westrenen, W.; Péraudeau, G.; Jaumann, R.; Seboldt, W. A brief review of chemical and mineralogical resources on the Moon and likely initial in situ resource utilization (ISRU) applications. *Planet. Space Sci.* **2012**, *74*, 42–48. [CrossRef]
14. Neill, T.; Judd, D.; Veith, E.; Rousar, D. Practical uses of liquid methane in rocket engine applications. *Acta Astronaut.* **2009**, *65*, 696–705. [CrossRef]
15. Salgado, M.C.V.; Belderrain, M.C.N.; Devezas, T.C. Space propulsion: A survey study about current and future technologies. *J. Aerosp. Technol. Manag.* **2018**, *10*, e1118.
16. Tajmar, M. *Advanced Space Propulsion Systems*; Springer Science & Business Media: Berlin/Heidelberg, Germany, 2012.
17. Baiocco, P. Overview of reusable space systems with a look to technology aspects. *Acta Astronaut.* **2021**, *189*, 10–25. [CrossRef]
18. Seedhouse, E. The Rise of the Falcon. In *SpaceX: Starship to Mars—The First 20 Years*; Springer International Publishing: Cham, Switzerland, 2022; pp. 58–70.

19. Dutheil, J.P.; Boué, Y. Highly reusable LOx/LCH4 ACE rocket engine designed for SpacePlane: Technical Maturation progress via key system demonstrators results. In Proceedings of the 7th European Conference for Aeronautical and Space Sciences, Milan, Italy, 3–6 July 2017.
20. Klem, M.D. LOX/Methane In-Space Propulsion Systems Technology Status and Gaps. In Proceedings of the Southwest Emerging Technology Symposium (SETS) 2017 (No. GRC-E-DAA-TN40702), El Paso, TX, USA, 1 April 2017.
21. Feng, S.; Nie, W.; He, B.; Cheng, Y. Three-Dimensional Numerical Simulations of Low Frequency Combustion Instability in a LOX/Methane Rocket Engine. In Proceedings of the AIAA SPACE 2010 Conference & Exposition, Anaheim, CA, USA, 27–30 September 2010; p. 8776.
22. Haidn, O.; Oschwald, M.; Clauss, W.; Arnold, R.; Sender, J.; Preuss, A.; Preclik, D.; Mäding, C.; Görgen, J.; Soller, S. LOx/Methane technology efforts for future liquid rocket engines. In Proceedings of the 5th International Spacecraft Propulsion Conference & 2nd International Symposium on Propulsion for Space Transportation, Crete, Greece, 5–8 May 2008.
23. Taya, K.; Ishikawa, Y.; Kimoto, K.; Ishizaki, S. Development status of LOX/LCH4 rocket engine. In Proceedings of the 50th AIAA/ASME/SAE/ASEE Joint Propulsion Conference, Cleveland, OH, USA, 28–30 July 2014; p. 3480.
24. Zurbach, S.; Thomas, J.L.; Sion, M.; Kachler, T.; Vingert, L.; Habiballah, M. Recent advances on LOX/methane combustion for liquid rocket engine injector. In Proceedings of the 38th AIAA/ASME/SAE/ASEE Joint Propulsion Conference & Exhibit, Indianapolis, Indiana, 7–10 July 2002; p. 4321.
25. Brown, T.; Klem, M.; McRight, P. Foundational Methane Propulsion Related Technology Efforts, and Challenges for Applications to Human Exploration Beyond Earth Orbit (No. M16-5248). In Proceedings of the Space Propulsion 2016, Roma, Italy, 2–6 May 2016.
26. Tao, F.; Xiao, B.; Qi, Q.; Cheng, J.; Ji, P. Digital twin modeling. *J. Manuf. Syst.* **2022**, *64*, 372–389. [CrossRef]
27. Jiang, L.; Su, S.; Pei, X.; Chu, C.; Yuan, Y.; Wang, K. Product-part level digital twin modeling method for digital thread framework. *Comput. Ind. Eng.* **2023**, *179*, 109168. [CrossRef]
28. Wang, T.; Tan, C.; Huang, L.; Shi, Y.; Yue, T.; Huang, Z. Simplexity testbed: A model-based digital twin testbed. *Comput. Ind.* **2023**, *145*, 103804. [CrossRef]
29. Aláez, D.; Olaz, X.; Prieto, M.; Villadangos, J.; Astrain, J.J. VTOL UAV digital twin for take-off, hovering and landing in different wind conditions. *Simul. Model. Pract. Theory* **2023**, *123*, 102703. [CrossRef]
30. Kim, S.; Im, J.H.; Kim, M.; Kim, J.; Kim, Y.I. Diagnostics using a physics-based engine model in aero gas turbine engine verification tests. *Aerosp. Sci. Technol.* **2023**, *133*, 108102. [CrossRef]
31. Xiong, M.; Wang, H.; Fu, Q.; Xu, Y. Digital twin–driven aero-engine intelligent predictive maintenance. *Int. J. Adv. Manuf. Technol.* **2021**, *114*, 3751–3761. [CrossRef]
32. Liu, Z.; Blasch, E.; Liao, M.; Yang, C.; Tsukada, K.; Meyendorf, N. Digital twin for predictive maintenance. NDE 4.0, Predictive Maintenance, Communication, and Energy Systems: The Digital Transformation of NDE. *Proc. Spie* **2023**, *12489*, 27–37.
33. Aivaliotis, P.; Georgoulias, K.; Chryssolouris, G. The use of Digital Twin for predictive maintenance in manufacturing. *Int. J. Comput. Integr. Manuf.* **2019**, *32*, 1067–1080. [CrossRef]
34. Matulić, N. Combustion Engine Digital Twin Development and Application Methodology for Real Time Diagnostic Systems. Ph.D. Thesis, Faculty of Electrical Engineering, Mechanical Engineering and Naval Architecture, University of Split, Split, Croatia, 2020. Available online: https://data.fesb.unist.hr/documents/public/Kvalifikacijski_Matulic.pdf (accessed on 20 December 2024).
35. Rosen, R.; Von Wichert, G.; Lo, G.; Bettenhausen, K.D. About the importance of autonomy and digital twins for the future of manufacturing. *IFAC-PapersOnLine* **2015**, *48*, 567–572. [CrossRef]
36. Jimenez Mena, D.; Pluchart, S.; Mouvand, S.; Broca, O. Rocket engine digital twin–modeling and simulation benefits. In Proceedings of the AIAA Propulsion and Energy 2019 Forum, Indianapolis, Indiana, 19–22 August 2019; p. 4114.
37. Vazquez, O. Trade Study Analysis of the Janus Moon Lander Vehicle. Ph.D. Thesis, The University of Texas at El Paso, El Paso, TX, USA, 2022.
38. Herrera, M.; Chaidez, M.; Welsh, Z.; Adams, J.; Bugarin, L.I.; Chessa, J.; Choudhuri, A.R. Design and Testing of a 500 lbf Liquid Oxygen/Liquid Methane Engine. In Proceedings of the AIAA Propulsion and Energy 2019 Forum, Indianapolis, Indiana, 19–22 August 2019; p. 3937.
39. Orozco Martinez, S.; Hernandez, I.; Hossain, M.A.; Choudhuri, A. Thermo-Structural Dynamics of the CROME Propulsion System: A Preliminary Study. In Proceedings of the AIAA SCITECH 2025 Forum, Orlando, FL, USA, 6–10 January 2025; p. 2340.
40. Trillo, J.E. Design of a 500 Lbf Liquid Oxygen and Liquid Methane Rocket Engine for Suborbital Flight. Master's Thesis, University of Texas at El Paso, El Paso, TX, USA, 2016; p. 767.
41. Hossain, M.A.; Morse, A.; Hernandez, I.; Quintana, J.; Choudhuri, A. Liquid Rocket Engine Performance Characterization Using Computational Modeling: Preliminary Analysis and Validation. *Aerospace* **2024**, *11*, 824. [CrossRef]
42. Welsh, Z.W. Qualification and Implementation of A Liquid Oxygen/Liquid Methane Data Acquisition System. Master's Thesis, Department of Mechanical Engineering, The University of Texas at El Paso, El Paso, TX, USA, 2020.
43. Hansen, C.G. Design Specifications and Requirements for a Mobile Data Acquisition System. Master's Thesis, Department of Mechanical Engineering, The University of Texas at El Paso, El Paso, TX, USA, 2019.

44. Rojo, R.M. Development and Implementation of the tRIAC Data Acquisition and Control System. Master's Thesis, Department of Mechanical Engineering, The University of Texas at El Paso, El Paso, TX, USA, 2019.
45. Pizzarelli, M.; Betti, B.; Nasuti, F.; Ricci, D.; Roncioni, P.; Battista, F.; Salvatore, V. Cooling channel analysis of a LOX/LCH4 rocket engine demonstrator. In Proceedings of the 50th AIAA/ASME/SAE/ASEE Joint Propulsion Conference, Cleveland, OH, USA, 28–30 July 2014; p. 4004.
46. Liberatori, J.; Malpica Galassi, R.; Liuzzi, D.; Filosa, A.; Valorani, M.; Ciottoli, P.P. Injection of LOX spray in Methane cross-flow RANS modeling uncertainty quantification. In Proceedings of the AIAA Propulsion and Energy 2021 Forum, Virtual Event, 9–11 August 2021; p. 3570.
47. De Giorgi, M.G.; Sciolti, A.; Ficarella, A. Application and comparison of different combustion models of high pressure LOX/CH4 jet flames. *Energies* **2014**, *7*, 477–497. [CrossRef]
48. Siemens. Star CCM+ User's Manual. Ver. 2021.3. New Features and Enhancements. Available online: https://www.aerofem.com/assets/files/Simcenter-STAR-CCM-2021.3-New-features-List-Fact-Sheet.pdf (accessed on 20 December 2024).
49. Vashahi, F.; Dafsari, R.A.; Rezaei, S.; Lee, J.K.; Baek, B.J. Assessment of steady VOF RANS turbulence models in rendering the internal flow structure of pressure swirl nozzles. *Fluid Dyn. Res.* **2019**, *51*, 045506. [CrossRef]
50. Ye, W.; Pan, Y.; He, L.; Chen, B.; Liu, J.; Gao, J.; Wang, Y.; Yang, Y. Design with modeling techniques. In *Industrial Ventilation Design Guidebook*; Academic Press: Cambridge, MA, USA, 2021; pp. 109–183.
51. Zhou, W.; Chen, B.; Zhu, Q.; Rao, S.; Xu, X. Numerical simulation of angled-injected liquid jet breakup in supersonic crossflow by a hybrid VOF-LPT method. *Int. J. Multiph. Flow* **2023**, *166*, 104503. [CrossRef]
52. Cui, L.; Chen, Z.; Feng, Y.; Li, G.; Liu, J. An improved VOF method with anti-ventilation techniques for the hydrodynamic assessment of planing hulls-Part 2: Applications. *Ocean Eng.* **2021**, *237*, 109505. [CrossRef]
53. Wang, J.H.; Luo, J.; Huang, S.X.; Xia, J.; Yang, B.; Wang, Y. Numerical simulation of single aluminum droplet evaporation based on VOF method. *Case Stud. Therm. Eng.* **2022**, *34*, 102008. [CrossRef]
54. Majumdar, A.; Valenzuela, J.; LeClair, A.; Moder, J. Numerical modeling of self-pressurization and pressure control by a thermodynamic vent system in a cryogenic tank. *Cryogenics* **2016**, *74*, 113–122. [CrossRef]
55. Qin, X.; Li, P.; Sun, P.; Huang, Y. Testing and comparison of a thermodynamic vent system operating in different modes in a liquid nitrogen tank. *Appl. Therm. Eng.* **2021**, *197*, 117393. [CrossRef]

Disclaimer/Publisher's Note: The statements, opinions and data contained in all publications are solely those of the individual author(s) and contributor(s) and not of MDPI and/or the editor(s). MDPI and/or the editor(s) disclaim responsibility for any injury to people or property resulting from any ideas, methods, instructions or products referred to in the content.